

Identification of Thioredoxin-Interacting Protein as a Potential Mediator of Anoikis-Resistance in Ovarian Cancer

THESIS

Presented in Partial Fulfillment of the Requirements for the Degree Master of Science in the Graduate School of The Ohio State University

By

Douglas Michael Spaeth-Cook Jr.

Graduate Program in Public Health

The Ohio State University

2017

Master's Examination Committee:

Courtney Hebert, Advisor

Randi Foraker

James Chen

Copyright by
Douglas Michael Spaeth-Cook Jr.
2017

Abstract

Epithelial ovarian cancer (EOC) is most commonly diagnosed at advanced stages, resulting in poor prognoses. Unlike most cancers, EOC does not typically spread hematogenously or lymphatically, opting instead for passive diffusion into the peritoneal cavity. This paper proposes a model that simulates the transition from primary tumor to disseminated disease using adherent and non-adherent cell culture conditions. Temporal transcriptomic analysis was performed on a well-studied ovarian cancer cell line that was subjected to this model. This resulted in the identification of TXNIP as a primary gene of interest. To validate the significance of this gene, a TXNIP knockdown cell line was developed using shRNA. Spheroid formation of the knockdown cell line *in vitro* was analyzed qualitatively and quantitatively using live-cell imaging. The knockdown was found to exhibit an anoikis-resistant phenotype. To assess prognostic relevance of the gene, the TCGA ovarian cancer dataset was queried for differences in patient survival outcomes based on categorization of high or low TXNIP expression in tumor samples, relative to median expression, at the time of initial surgery. High TXNIP expression was found to correlate significantly with longer overall and progression free survival in early stage patients. The same was not true for late stage patients. To assess the effect of platinum agents on TXNIP, carboplatin was used to treat three ovarian cancer cell lines grown in non-adherent conditions for 48 hours. Western blots confirmed that 100 nM

carboplatin did not affect TXNIP expression at 48 hours. The findings of this paper lead us to believe that TXNIP is a potential mediator of anoikis-resistance in ovarian cancer.

Dedication

This document is dedicated to Jason and Joel David.

Acknowledgments

I would like to thank everyone in the Hays, Chen, Strohecker, and Pollock labs. I could not have completed this project without the help you have given me over the past two years. A special thank you to John Hays and James Chen for your mentorship, guidance, and understanding. Thank you to Courtney Hebert for advising me academically and participating on my thesis committee. Thank you to Randi Foraker for participating on my thesis examination committee and for instructing me in epidemiology. Thank you to James Gentry. Thank you to everyone working on the 5th floor at BRT.

Thank you to John Hays and James Chen for assisting me with the methods and analyses presented in this paper. Thank you to Mark Burch for developing the outlier identification technique used in this paper.

Vita

June 2007Bexley High School
2012.....B.A. Chemistry, Miami University
2013B.S. Pharmaceutical Sciences, The Ohio
State University
2015 to presentGraduate Research Associate, Department
of Biomedical Informatics, The Ohio State
University

Publications

Chen JL, David J, Cook-Spaeth D, Casey S, Cohen D, Selvendiran K, et al. Autophagy Induction Results in Enhanced Anoikis Resistance in Models of Peritoneal Disease. Mol Cancer Res. 2017 Jan;15(1):26–34.

Fields of Study

Major Field: Public Health

Specialization: Biomedical Informatics

Table of Contents

Abstract	ii
Dedication	iv
Acknowledgments	v
Vita	vi
Publications	vi
Fields of Study	vi
List of Tables	viii
List of Figures	ix
Chapter 1: Introduction	1
Chapter 2: Background	2
Chapter 3: Methods	11
Chapter 4: Results	20
Chapter 5: Discussion	24
References:	29
Appendix A: Tables and Figures	32

List of Tables

Table 1: Images acquired per experiment.....	49
Table 2: Results of t-tests.....	50

List of Figures

Figure 1: Model of peritoneal metastasis.....	32
Figure 2: Overview of study design.....	33
Figure 3: Z-stack generated with confocal microscopy	34
Figure 4: Example of pixel masking.....	35
Figure 5: Image analysis workflow.....	36
Figure 6: ImageJ macro	37
Figure 7: Inter-experimental variability in non-adherent conditions	38
Figure 8: Averages of total spheroid area versus time.....	39
Figure 9: Beeswarm plots	40
Figure 10: Clustering	41
Figure 11: TXNIP mRNA expression versus time in non-adherent conditions.	42
Figure 12: Western blots of knockdown versus control	43
Figure 13: Three-dimensional reconstruction of HeyA8 spheroids.....	44
Figure 14: Comparisons of knockdown and control at 48 hours	45
Figure 15: Plot of confluency versus time for knockdown and control.....	46
Figure 16: Kaplan-Meier plots.....	47
Figure 17: Western blot showing effect of carboplatin on TXNIP expression.....	48

Chapter 1: Introduction

Currently, there are no effective population-wide screening methods for epithelial ovarian cancer (EOC). Consequently, EOC is most commonly diagnosed at advanced stages. Most EOC patients present with ascites and the disease is known to disseminate via the peritoneal cavity, leading to peritoneal carcinomatosis and metastasis. To aid in the identification of new targeted therapies that increase survival rates, the development of realistic *in vitro* models of EOC progression are necessary. This paper proposes a model that simulates the transition from primary tumor to disseminated disease using adherent and non-adherent cell culture conditions. In this study, we use temporal transcriptomic analysis to sort genes into clusters and identify outlying genes which we then investigate further. We hypothesized that these outlying genes would play a modulatory role in anoikis-resistance mechanisms in the early stages of tumorsphere formation.

The aims of this study are to: 1) refine an *in vitro* model of ovarian cancer metastasis, 2) use bioinformatics methods to identify potential drivers of anoikis-resistance in ovarian cancer, 3) develop imaging techniques to study tumorsphere formation and growth kinetics, and 4) validate findings using *in vitro* experiments.

Chapter 2: Background

Ovarian Cancer Epidemiology

Ovarian cancer (OC) is a deadly, heterogeneous disease. According to results from the National Cancer Institute's Surveillance, Epidemiology, and End Results Program (SEER), OC is currently the fifth most lethal cancer type affecting women in the United States. The disease has a 5-year survival rate close to 46.5% and its incidence was estimated to be approximately 11.7 cases per 100,000 women from 2010-2014. The median age of diagnosis from 2010-2014 was 63 years of age and approximately 75% of incident OC cases were diagnosed at advanced stages (1). Due to the relatively low incidence of OC along with the low positive predictive value of current screening tests reliant upon on transvaginal ultrasound and CA-125 measurements, as of 2012, the U.S. Preventive Services Task Force does not recommend screening of asymptomatic women who are not considered high-risk (2). Risk factors for OC include age, use of fertility drugs, hormone therapy for menopause, and BRCA1/2 mutations. Several factors have been found to be protective including parity, breastfeeding, and contraceptive use (3). Epithelial ovarian cancer (EOC) is a common subtype of OC that presents most frequently in post-menopausal women with symptoms including several months of abdominal pain and distension. The most common cause of death from EOC is bowel obstruction (4). EOC can also be broken down further into several morphological

subtypes including high-grade serous, mucinous, endometrioid, and clear cell. These subtypes are determined after pathological analysis, but at least one recently conducted study in 2015 was partly successful in identifying EOC subtypes based on imaging alone (5).

Staging

The International Federation of Gynecology and Obstetrics (FIGO) staging system is used in the diagnosis and treatment of EOC (6,7). Clinical staging is done prior to treatment. It is considered preliminary and less accurate than the surgical staging because it is based on an incomplete picture of the cancer. Surgical staging, on the other hand, is done at the time of initial surgery and is based on direct visual inspection and pathological analysis of tumor tissue and ascitic fluid. Grading of one through three is also done after surgery, with grade one being the most like normal tissue and grade three being the fastest growing and least like normal tissue. Ascitic fluid is analyzed for the presence of tumor spheroids and microscopic metastasis. Stage one EOC is a tumor that has not spread beyond the ovaries. Stage one can be further classified based on whether the cancer is unilateral, bilateral, or if the ovarian capsule has ruptured. Stage two EOC indicates that the cancer has spread to other tissues within the pelvic region. Stage two can be further classified based on which pelvic tissues or organs the cancer has infiltrated. Stage three EOC indicates spread to tissues adjacent the pelvic region or to retroperitoneal lymph nodes. Stage three can be further classified based on which tissue

has been invaded and the size of the tumor that has spread. Stage four EOC indicates that the cancer has spread to distant sites.

Treatment

Initial treatment for EOC is dependent on stage, performance status, and the patient's desire to maintain fertility (6,7). Surgical staging is the first phase of treatment. Most advanced stage cancers, other than ovarian, do not obtain survival benefits from debulking procedures, thus EOC is special in that debulking surgery works to improve survival (8). During surgical staging the cancer will be staged and surgeons will remove as much disease as possible. Surgical staging may also involve complete removal of the patient's omentum, ovaries, fallopian tubes, uterus, and cervix. Both platinum-based and taxane-based chemotherapy are recommended if the cancer is beyond stage 1. Advanced stage disease is treated with either intraperitoneal (IP) or intravenous (IV) chemotherapy following surgery. IP chemotherapy is injected directly into the peritoneal cavity via a catheter and port. It has pharmacokinetic advantages over IV delivery that can make it preferable in situations where the disease has not spread systemically (9). IP delivery is associated with increased toxicity as compared to IV delivery and is therefore not recommended for use in patients with low performance status. IP delivery is not used in stage 4 patients. Patients typically undergo 4 to 8 cycles of chemotherapy after surgery. Each cycle typically lasts between 7 and 21 days. In some cases, chemotherapy may be given in advance of surgery in an attempt to shrink tumors so that they can be more easily resected during surgery. If patients relapse within 6 months of chemotherapy they are

considered to be platinum-resistant. Otherwise, they are considered platinum-sensitive and will be candidates for further platinum-based treatment if they relapse.

Peritoneal Metastasis

The most common site for metastasis in EOC is the peritoneal cavity. Malignancy-related ascites is a potential consequence of peritoneal metastasis. Abnormally high levels of ascitic fluid accumulate due to blockages that form in lymphatics. Increased vascular permeability due to tumor secretion of vascular endothelial growth factor is also a major contributing factor (10). Glucose concentrations within ascites are assumed to be similar to serum blood glucose levels. This supposition is supported by several studies that have shown ascitic glucose conditions to be less than or equal to normal physiologic serum concentrations of 70-100 mg/dL. One study of 43 patients with confirmed malignant ascites reported an average glucose concentration of 95 mg/dL (11). Another study, using H-NMR spectroscopy for quantitative estimation of glucose concentration, found that patients with malignant, cancerous ascites had significantly lower ($p < 0.01$) glucose concentration of 55.8 mg/dL (4933 ± 2980 uM) as compared to patients with benign ascites due to cirrhosis. The patients with benign ascites exhibited average ascitic glucose concentrations of 95.14 mg/dL (8411 ± 4886 uM) (12). In a 2013 longitudinal study of 333 patients with EOC, ascites occurred in 78% of the cases overall. Ascites was present in 50.6% of stage I patients, 62.5% (stage II), 90.1% (stage III), and 100% (stage IV). The volume of ascites was found to be significantly positively correlated with stage ranging from less than 100 mL to 3,800 mL at the point of primary treatment (13).

Treatment of ascites in practice is solely for the relief of ascites-related symptoms including abdominal pain, shortness of breath, and gastrointestinal upset (10).

Paracentesis is performed to reduce ascitic volume and it frequently requires repeated treatments. Interestingly, when patients who were given palliative peritoneovenous shunts to help relieve symptoms associated with ascites, cancer was found to metastasize to the same areas as would be expected if there were not systemic distribution of tumor cells.

Patients diagnosed with stage 1C EOC have lower overall survival as compared to stage 1A or 1B. This is most likely due to the occult presence of tumor in the ascites. One study showed that cells taken from metastatic deposits were strikingly similar to primary tumor as evidenced by their overlapping gene expression profiles. The study reported that there were only 64 differentially expressed genes between the primary and metastatic tumor tissue that they analyzed. This has led to the hypothesis that at least some metastatic sites are monoclonal as opposed to polyclonal in origin.

The Cancer Genome Atlas Ovarian Dataset

The Cancer Genome Atlas Project (TCGA) was established in 2005 with the aim of generating and analyzing large-scale, publicly available, genomic datasets for a variety of cancers. TCGA is managed by the National Cancer Institute (NCI) and the National Human Genome Research Institute (NHGRI). The project is funded by the NCI, NHGRI, and federal funds allocated via the American Recovery and Reinvestment Act of 2009

(ARRA) (14). Ovarian cancer was characterized in the first phase of TCGA (15). As of 2014, few of the gene-expression based biomarkers identified in TCGA studies have found their way into clinical practice. There are conflicting views on how useful the TCGA findings have been in their ability to help predict prognosis. One study, published in Nature, attempted to assess the added prognostic benefit of including molecular data together with clinical variables. The study found that molecular biomarkers added very little to prognostic stratification (16). Alternatively, a 2008 study using data from the tumor bank ovarian cancer network (TOC), successfully used semi-supervised prediction methods to validate the ability for TCGA generated ovarian molecular markers to predict prognosis independently from clinical variables alone (17). Having good prognostic information for response to standard treatment of platinum and taxane combinations would be useful in identifying patients who might respond better to new experimental treatments.

As of 2017, the TCGA ovarian cancer dataset includes 608 cases. Tissue samples were resected from newly diagnosed patients prior to any treatment for the disease at tissue source sites including: Memorial Sloan-Kettering, Washington University, University of Pittsburgh, Mayo Clinic, Duke University, Gynecologic Oncology Group, Cedars-Sinai Medical Center, University of California San Francisco, Harvard Medical School, MD Anderson Cancer Center, British Columbia Cancer Agency, Fox Chase Cancer Center, Imperial College London, International Genomics Consortium, and Roswell Park Cancer Institute (18). Specimen acquisition was standardized and quality control measures were

implemented to ensure consistency in collection methods across sites. Once collected, samples were sent to a biospecimen core resource for inspection and storage. Only about half of the samples sent to the biospecimen core resource have passed quality control tests for inclusion into the dataset. Clinical data was collected for each case at the respective tissue source site and sent to the biospecimen core resource for electronic data entry. Surgical cytoreduction was recorded as optimal (microscopic or less than or equal to 1 cm diameter residual disease) or suboptimal (greater than 1cm or residual disease). The TCGA study found that the detection of microscopic residual disease (less than 0.1 cm) was significantly associated with longer overall survival, as compared to patients with optimally debulked disease. However, there was no statistically significant difference found in optimally versus suboptimally debulked disease. Three platforms were used for gene expression measurement in each sample including Agilent, AffymetrixHuEx, and Affymetrix U133A.

TXNIP

The thioredoxin interacting protein (TXNIP) gene encodes for a 391 amino acid protein that is named for its ability to bind and mediate thioredoxin (19). TXNIP has also been shown to bind to importin- α , NLRP3, Mybbp1a, Jab1, SMRT-mSin3-HDAC, and REDD1 (20–22). It is known to be upregulated by 1,25-dihydroxyvitamin D and is, consequently, also known as vitamin D-regulated gene (VDUP-1). TXNIP protein can be found in a variety of intracellular locations including the cytosol, nucleus, and mitochondria. Its localization is deeply connected to oxidative stress (23–25).

Functionally, TXNIP is known to be involved oxidative stress response, glucose regulation, autophagy, and apoptosis. Downregulation of TXNIP results in increased glucose uptake and increased reliance on glycolysis by triple-negative breast cancer cells. Conversely, upregulation of TXNIP has been shown to lead to a significant decrease in cellular glucose uptake (26). The role that TXNIP plays in cancer is complex. TXNIP is currently thought to be a tumor suppressor because higher TXNIP expression has correlated with better survival outcomes in breast cancer, hepatocellular carcinoma, bladder cancer, and leukemia (27). And yet, according to a study published in 2015, increased expression of TXNIP was significantly correlated with shorter progression free survival in a cohort of 70 non-small cell lung cancer patients (28).

Spatial Conceptualization of Tumor Spheroids

Three-dimensional *in vitro* tumor models may provide a more accurate representation of *in vivo* cancer biology as compared to traditional two-dimensional cell culture models (29–31). 3D systems generate multicellular aggregates (Figure 1), also referred to as spheroids or tumorspheres, that provide individual cells with a 3D spatial architecture. This 3D architecture is arguably more representative of an *in vivo* environment as compared to a 2D monolayer of cells because *in vivo* tumors do not grow in monolayers. Gene expression profiles of cells in 3D systems have been shown vary considerably from the same cell types grown in 2D systems. Genomic and physical differences lead to significant phenotypic differences in drug response and cell survival. These differences can be attributed to the physical architecture that is created by multicellular tumor

spheroids. These models are not a replacement for *in vivo* models. One study examined the differences between the same cell line grown in 2D, two different 3D models, and in mice and found that there were substantial gene expression differences across all models (32). This means that 3D systems are not always more representative than 2D systems. All *in vitro* systems lack some component present in an *in vivo* system such as vascularization or other cell types.

Chapter 3: Methods

Study design

An outline of the study design can be found in Figure 2. In brief, RNA was isolated from spheroids every 6 hours over a 72 hour time course. Next, samples were frozen and shipped in dry ice to University of Chicago for gene expression measurement using microarray chips. Next, genes were clustered based on trends in their temporal expression and outlier genes were ranked based on each gene's Mahalanobis distance from its nearest cluster centroid. A literature review was then conducted to assess biological relevance of the gene. Next, the gene was assessed for prognostic differences using the TCGA ovarian cancer dataset. Next, a shRNA knockdown of the lead outlying gene was developed along with a scrambled control. Finally, the knockdown and control cell line were analyzed for differences in growth kinetics using live-cell imaging and measurement of protein expression.

Cell culture

HeyA8 cells were maintained in T-75 flasks at 5% CO₂ and 37 Celsius using RPMI 1640 media supplemented with L-Glutamine (ThermoFischer, cat#11875093), 1% Penicillin-Streptomycin (ThermoFischer, cat#15070063), and 10% Fetal Bovine Serum (ThermoFischer, cat#10438026). Glucose concentration of cell culture media was 220

mg/dL due to RPMI 1640 and Fetal Bovine Serum. Cells were passaged at 80% confluency and were not kept beyond passage 10.

Attachment-independent conditions for protein collection

Cells were grown in 6 well flat-bottom plates coated with poly-2-hydroxyethyl methacrylate, also known as polyHema (Sigma-Aldrich, cat#1920660), after being seeded at a cell density of 62,500 cells per cm². Glucose concentrations were controlled to better represent physiologic ascites conditions. Three independent glucose conditions were used. The glucose conditions were designated: “full” (220 mg/dL), “half” (110 mg/dL), and “none” or “no glucose” (less than 20 mg/dL). The 110 mg/dL glucose concentration was obtained by mixing full glucose RPMI 1640 (ThremoFischer, cat#11875093) with glucose-free RPMI 1640 (ThremoFischer, cat#111879020).

Attachment-independent conditions for time-lapse imaging

Cells were grown in 96 well flat bottom plates coated with poly-2-hydroxyethyl methacrylate (polyHema) after being seeded at a cell density of 62,500 cells per cm². Glucose concentrations were controlled to better represent physiologic ascites conditions. Three independent glucose conditions were used. The glucose conditions were designated: “full” (220 mg/dL), “half” (110 mg/dL), and “none” or “no glucose” (less than 20 mg/dL). The 110 mg/dL glucose concentration was obtained by mixing full glucose RPMI 1640 (ThremoFischer, cat#11875093) with glucose-free RPMI 1640 (ThremoFischer, cat#111879020).

mRNA expression time-course using gene microarray

HeyA8 cells were trypsinized with 0.25% Trypsin-EDTA, counted using a hemocytometer, and subsequently seeded in triplicate in polyHema coated 6 well plates. Lysates were isolated using a Qiagen RNeasy kit every 6 hours for 72 hours post seeding. The quality of RNA samples was checked using a NanoDrop spectrophotometer. Samples were analyzed using an Illumina HT-12 platform and later processed with GenomeStudio (Illumina).

Gene expression profile analysis

Gene expression values from the above microarray data were clustered using a Gaussian Mixture Model. After normalizing all timepoints to the time zero gene expression level, time variant outlying genes were identified using a Mahalanobis Distance metric. These genes showed the highest deviance from clusters identified using the Gaussian Mixture Model.

Immunoblotting

Cells were seeded in 6 well polyHema coated plates or 6 well standard cell culture flasks, depending on what condition was being tested. Cells were lysed with cold RIPA buffer and transferred to 1.5 mL microtubes. Lysate was kept on ice and vortexed gently 3 times for 15 seconds. Lysate was centrifuged at 15,000 RPM for 20 minutes at 4 Celsius. The resulting supernatant was saved and stored at -20 Celsius. After all samples were collected, lysates were thawed and protein was quantified using a Direct Detect

Spectrometer (EMD Millipore). Samples were mixed with distilled water and Laemmli Sample buffer to obtain 20 µg concentrations. Next, samples were heated for 5 minutes at 100 Celsius. Samples were loaded into mini-PROTEAN precast gels (Bio-Rad). Gels were run in tris/glycine buffer at 300 volts. Protein was transferred onto PVDF blots using a Trans-Blot Turbo system (Bio-Rad). Following transfer, the blots were left to dry for 45 minutes before blocking with PBS based blocking buffer (Licor). After blocking at room temperature for one hour, blocking solution was removed. Primary antibodies were then added and incubated at 4 Celsius overnight. After removal of primary antibodies, blots were washed with PBS-Tween 0.01% for 5 minutes, 3 times. Next, near-infrared fluorophore secondary antibodies (Licor) corresponding to the primary antibody type were added and incubated for 1 hour at room temperature. Blots were imaged dry using an Odyssey CLx near-infrared imaging system. Brightness and contrast of resulting images were adjusted using Image Studio Lite 5.0. Pixel densitometry was performed by, first, normalizing each loading control signal to the first lane loading control signal. Next, the target protein signals for each lane were multiplied by the normalized loading control signal for that lane. Fold-changes between lanes were calculated from the resulting values.

shRNA knockdown of TXNIP

Low-passage HeyA8 cells were grown as adherent cells as described above.

Transfection-ready TXNIP Human shRNA plasmids with a green fluorescent protein tag (Origene, cat#TG308550) were added to HeyA8s by following manufacturer protocol.

The best one out of four constructs was used for all experiments. The best construct was selected based on confirmatory western blots to ensure maximum silencing effect. It is referred to as TXNIP-KD, TXNIPKD, and TXNIP knockdown throughout this paper. A control cell line was also generated using a transfection-ready 29-mer scrambled shRNA construct encased in a green fluorescent protein vector. The control cell line is referred to as HeyA8 scrambled throughout this paper.

High-content confocal imaging of non-adherent cells

Low-passage HeyA8 scrambled cells were seeded in several wells of an ultra-low attachment 96 well plate (Corning, cat#3474). Cells were placed in a climate controlled chamber (5% CO₂ and 37 Celsius) and imaged every 4 hours on DIC and green channels using a Nikon A1R Live Cell Imaging Confocal microscope to monitor the spheroid formation process. Tiled images of each z-plane were assembled using Metamorph Premier Plus (Molecular Devices). Z-stacks were assembled using ImageJ (NIH) and NIS-Elements (Nikon) to create a three-dimensional image of a single well that could be viewed and manipulated using ImageJ (Figure 3).

Time-lapse imaging of adherent cells

Low-passage HeyA8 scrambled and HeyA8 TXNIP-KD cells were seeded in 96 well plates at 4,000 cells per well. The plates were then transferred to an IncuCyte ZOOM live-cell microscope (Essen Bioscience) housed in an incubator. Cells were maintained at 5% CO₂ and 37 Celsius. Phase-contrast and green channel images were taken of each

well using a 10x Nikon objective. Images were tiled and stitched by the IncuCyte ZOOM software (version 2015A). Masking of adherent cells was also done by the IncuCyte Zoom software using only the phase-contrast channel. Green channel images were not used due to phase images showing superior masking (Figure 4). Data was exported to Excel 2016 and a graph of percent confluence versus time was generated for the scrambled and knockdown cell lines. An unpaired t-test was conducted using Prism 7.0 based on the 48 hour time point for each condition to assess differences in mean confluency (Table 2).

Whole well time-lapse imaging of non-adherent cells

Low-passage HeyA8 scrambled and HeyA8 TXNIP-KD cells were seeded in 96 well plates at 20,000 cells per well. The plates were then transferred to an IncuCyte ZOOM live-cell microscope (Essen Bioscience) housed in an incubator. Cells were maintained at 5% CO₂ and 37 Celsius. Phase-contrast and green channel images were taken of each well using a 4x Nikon objective on whole well mode. The resulting images were then analyzed according to the image analysis workflow presented in Figure 5. Images were tiled and stitched by the IncuCyte ZOOM software (version 2015A). Analysis and masking of non-adherent cells was done using a custom script written for Fiji (33). Only data from the green channel was used in masking and analysis. Data was exported to Excel 2016 and Tableau Desktop for visualization.

Image analysis for non-adherent conditions

After acquisition by the IncuCyte Zoom system, images were stored locally on a network attached storage device and analyzed using the general workflow presented in Figure 5. Tiled images were stitched by IncuCyte Zoom software, if necessary. Image archives for each experiment were exported to an external hard drive as raw 16-bit .TIFF files.

Approximately 17,493 images were collected in total over 8 independent experiments using non-adherent conditions (see Table 1 for a breakdown of the number of images captured). Images were loaded into ImageJ using a custom script (Figure 6) in batches no greater than 1,000 images due to performance constraints of the computers being used for processing. We recommend using a computer with at least 8 gigabytes of memory and a solid state hard drive when running the ImageJ script. The batch process loaded “virtual stacks” of images instead of loading images directly into RAM. Frequently, if not always, the aggregate size of all images in a batch would far exceed the amount of RAM available. Virtual stacks load images directly from the hard drive instead of from RAM. This enables the user to load a greater number of files, with the downside being a substantial increase in the time it takes to load images for processing. However, considering that files would need to be loaded from the hard drive into RAM either way, the extra time it takes to process a virtual stack is almost irrelevant for batches with an aggregate file size greater than the amount of RAM available. After loading images as a virtual stack, thresholding was performed. Thresholding involves converting each pixel into a binary value of 1 or 0. If a pixel’s original intensity is above the threshold, it is marked as a one and therefore represents signal (i.e. belonging to part of a cell). On the

other hand, if the pixel's original intensity is below the threshold, it is marked as a zero to designate it as background (i.e. not belonging to part of a cell). After thresholding, the macro tasks ImageJ with counting all the pixels within an image that are above the threshold value. The macro prompts the user to save the results as an excel file that contains aggregate pixel counts for each image, one row per image. The resulting spreadsheet was cleaned and organized so that the data can be normalized. The following column names were generated in the final spreadsheet: originalLabel, totalArea, experimentID, wellCode, rowCode, columnCode, timepointHours, glucoseCond, cellLine, drugTreatment, throwAwayData, absRef, normalizedDataFormula, normalizedDataUseableValues, concatID, and Spheroid/Attached/Reattached. Normalization involved running a macro in Excel 2016 designed to assign absolute references to the "zero" timepoint for each timepoint associated with a given well. Each time point was then divided by the time zero fluorescence value of its particular well. Next, data was imported to Tableau Desktop for data visualization and qualitative analysis. Two experiments were excluded due to inconsistent masking. Inter-experimental variability was analyzed qualitatively in Tableau (Figures 7 and 8). A Welch's t-test was conducted using Prism 7.0 based on the 48 hour time point for each cell line grown in half glucose conditions (Table 2).

Survival outcomes analysis using TCGA dataset

KMPlotter (34) was used to split TCGA ovarian cancer data on median expression of TXNIP. Data was split into early (stage I and II) and late stage (stage III and IV) cohorts.

Survival curves were generated using KMPlotter. Only optimally debulked patients were selected for stage III and stage IV patients. The resulting log-rank p values comparing overall survival and progression free survival comparisons were reported. Hazard ratios and hazard ratio confidence intervals were also reported to assess the magnitude of effect. Finally, beeswarm plots were generated to assess distributions of transcript expression levels (Figure 9).

Chapter 4: Results

Identification of TXNIP as a primary gene of interest

TXNIP emerged as the top outlier in our Gaussian Mixture Model based on its measured Mahalanobis distance from its nearest cluster (Figure 10 and 11). A brief literature review of studies mentioning TXNIP revealed several accounts purporting it to be a tumor suppressor gene that was potentially mechanistically involved in a process known as autophagy. TXNIP's role in diabetes has also been studied extensively, which has led to the finding that the gene plays a major role in glucose regulation and response to oxidative stress. Based on this information, we decided to create a TXNIP shRNA knockdown cell line, in order to assess the gene's effect on spheroid growth kinetics. Successful knockdown of TXNIP and validation of transcriptomic findings were confirmed by western blot densitometry (Figure 12).

Characterization of spheroid formation dynamics

Live-cell confocal microscopy was used to create a three-dimensional image of all spheroids within a well (Figure 13). This was done in order to characterize spheroid morphology. We learned that HeyA8 spheroids frequently formed both ellipsoid and spherical clusters. Spheroid formation typically occurred at 13 hours post-seeding in non-adherent conditions. Spheroids generated *in vitro* were similar in size and

morphology to those found in samples of ovarian cancer patient ascites as previously reported by Chen et al (35).

Effect of TXNIP on spheroid proliferation

We tested HeyA8 scrambled and HeyA8 TXNIP-KD cells' ability to form spheroids in multiple different glucose concentrations. We found differences in spheroid proliferation when comparing the two cell lines (Figure 14). We believe that this inter-experimental variability could be minimized by using a more robust image thresholding algorithm. The algorithm that we used treated all images in the time series independently and we normalized each time point to the total fluorescence detected at time zero. This normalization procedure was found to be slightly problematic because cells were not always evenly dispersed at the time of seeding. Nonetheless, TXNIP-KD cells appear to grow and divide faster than scrambled cells over the first 48 hours in non-adherent conditions. An unpaired, two-tailed Welch's t-test was performed and the result was significant with $p < 0.05$. Even across glucose conditions, TXNIP-KD spheroids were larger by at least 20% (Figure 8).

Effect of TXNIP on growth kinetics in attached conditions

HeyA8 scrambled and HeyA8 TXNIP-KD cells were grown in standard 96 well flat bottomed plates. A graph of percent confluence versus time was generated for the scrambled and knockdown cell lines (Figure 15). Images were taken every hour for 48 hours and the resulting data was tested using a two-tailed unpaired t-test for difference in

means at the 48 hour timepoint. The result was significant at $p < 0.05$ (Table 2). The data showed that the scrambled condition had higher confluency at 48 hours than the knockdown condition (Figure 14).

Correlation of TXNIP expression levels with survival data from TCGA dataset

Patients within the TCGA EOC dataset were separated into early and late stage cohorts and split on median TXNIP expression level to assess survival differences using Kaplan Meier curves (Figure 16). Progression free survival in early stage disease was significantly different for at least one point on the survival curves based on a statistically significant log-rank p value of less than 0.05. The trend in progression free survival showed that early stage patients with TXNIP expression values above the median performed better. These patients experienced longer intervals before relapse after the completion of primary chemotherapy. As expected, the PFS findings matched overall survival findings. The early stage patients with higher TXNIP expression levels at the time of surgery progressed later and lived longer than early stage patients with lower TXNIP expression levels. Late stage patients with TXNIP expression levels above the median exhibited significantly shorter overall survival with a log-rank p value of 0.043. In late stage patients, PFS showed a similar trend to overall survival, but that trend was not statistically significant.

Protein expression of TXNIP is not affected by platinum agent

Three ovarian cancer cell lines (HeyA8, Ovar8, Skov3) were subjected to 100 nM carboplatin for 48 hours in non-adherent conditions. A western blot testing for TXNIP expression was performed on untreated and treated cells. The blot showed no significant alteration in TXNIP expression between untreated and treated cells of all three cell lines after 48 hours (Figure 17).

Chapter 5: Discussion

Part of the reason it is so important to research ovarian cancer is the peculiarity of the disease itself. Rather than spreading hematogenously or lymphatically like most cancers, ovarian cancer spreads transcoelomically. After the formation of a primary tumor, it is believed that certain populations of cancer cells detach from the original site and float into the peritoneal cavity. Normal cells, upon detachment, would immediately undergo a form of pre-programmed cell death termed anoikis. However, ovarian cancer cells avoid this self-regulating biological process and instead often develop into multicellular floating spheroids that continue to grow and eventually implant on peritoneal surfaces. These implantations invade surface tissue and overwhelm vital organs, disrupting bodily processes, leading in most cases to death.

Because of the direct danger associated with spheroids in advanced stage ovarian cancer, the study of spheroids *in vitro* is crucial to the development of better treatment methods. In this study, we modeled the spread of ovarian cancer using cells placed in attachment-free conditions. The HeyA8 cell line, a high grade serous adenocarcinoma subtype of ovarian cancer, formed spheroids when grown in non-adherent conditions. We used longitudinal microarray data generated using HeyA8 cells over the course of 72 hours post-detachment to identify genes that were least concordant with clusters. In doing so, TXNIP was identified as the leading outlier. In order to validate the *in vitro* relevance of

TXNIP we then generated a HeyA8 cell line with TXNIP knocked down by an shRNA construct. We also generated a HeyA8 control cell line using a scrambled vector. The promoters of the TXNIP and scrambled genes were tagged with a gene for green fluorescent protein. This enabled us to perform fluorescence image analysis with an adequately high signal-to-noise ratio.

The methods we used for image analysis led to the identification of statistically significant differences being found between the TXNIP-KD and scrambled cell line with respect to growth kinetics in attached and spheroid form. We noted trends that appeared to show the TXNIP-KD cell line exhibiting greater resistance to anoikis. This was concluded based on the relative size of spheroids at 48 hours post seeding.

The clinical relevance of the gene was further examined by splitting the TCGA ovarian cancer dataset into early and late stage cohorts and assessing the survival outcomes as a function of TXNIP expression. The finding that early stage patients with high TXNIP levels have longer overall survival is congruent with current literature that purports TXNIP to be a tumor suppressor gene. Interestingly, the late stage cohort was discordant with the early stage cohort with respect to which TXNIP category had longer overall survival. We found that later stage patients with higher TXNIP expression values had shorter overall survival. While it is not immediately clear as to why this might have occurred, it is worth noting that the differences in survival were relatively small. The TCGA dataset has far more late stage patients than early stage patients, which could have

helped late stage patients achieve statistically significant differences even though the magnitude of effect was small in comparison to early stage patients.

Finally, protein expression of three well-characterized high grade serous ovarian cancer cell lines was evaluated after treatment with 100 nM carboplatin for 48 hours in non-adherent conditions. Considering that carboplatin is the first line chemotherapeutic treatment for ovarian cancer, it is interesting that it has no effect on TXNIP expression. This finding suggests that it is worthwhile to explore modulating TXNIP pharmacologically as a potential alternative therapy for platinum-resistant tumors.

Limitations

There are several limitations present in this study. First, research into biomarkers is not easily integrated into clinical practice. Second, this study only validates one cell line. In addition, *in vitro* cell lines are notoriously unrepresentative of current real-world manifestations of disease. Third, the use of *in vitro* models cannot guarantee successful translation of results to *in vivo* conditions. Fourth, while the tissue procurement methods of the TCGA dataset were standardized, errors and variances in the application of these practices are still possible. Furthermore, to the extent of our knowledge, the TCGA collection protocol does not specify whether samples were extracted from primary or metastatic sites. Fifth, microarray data vary greatly across different platforms making relative comparisons difficult and sometimes impossible. To counter this, we validated microarray findings using analysis of protein expression through western blots. Sixth, in

order to utilize imaging methods in the analysis of spheroid growth dynamics, several limiting factors must be considered: timing of spheroid formation is frequently not consistent, modeling 3D growth using a 2D area involves substantial approximation, and differences in levels of fluorescence between cell lines occur. Seventh, the relationship between spheroid size and metastatic potential is unstudied. Finally, although we chose to frame our study in 72 hour period, the true relationship between time *in vivo* and time *in vitro* is unclear.

Conclusion

With the conclusion of this study, we have successfully described an *in vitro* model of ovarian cancer metastasis and applied bioinformatics methods to identify TXNIP as a potential driver of anoikis-resistance in ovarian cancer. Although we have begun the process of validating our findings using *in vitro* experiments, further refinement of our live-cell imaging analysis methodology is necessary to complete the process. Because many of the image analysis tools we used are open source, we hope other researchers will continue our endeavor to validate the bioinformatics methods developed in this study. We believe that identifying outlying genes as mediators of cancer-specific processes holds great promise for the future treatment of patients with ovarian cancer.

Public Health Relevance

Biomarker identification and validation are key areas to the advancement of public health and oncology research. Further development of techniques used to identify meaningful,

clinically relevant biomarkers will lead to better screening and diagnostic tests, more accurate prognostic assessments, and improved prediction of response to therapy.

References:

1. Noone A-M, Cronin KA, Altekruze SF, Howlader N, Lewis DR, Petkov VI, et al. Cancer Incidence and Survival Trends by Subtype Using Data from the Surveillance Epidemiology and End Results Program, 1992-2013. *Cancer Epidemiol Biomarkers Prev.* 2017 Apr;26(4):632–41.
2. Final Update Summary: Ovarian Cancer: Screening - US Preventive Services Task Force [Internet]. [cited 2017 Apr 21]. Available from: <https://www.uspreventiveservicestaskforce.org/Page/Document/UpdateSummaryFinal/ovarian-cancer-screening>
3. FACS RB, Berchuck A, MD MM, FACR MERM. Principles and Practice of Gynecologic Oncology. Sixth edition. Philadelphia: LWW; 2013. 1118 p.
4. Jayson GC, Kohn EC, Kitchener HC, Ledermann JA. Ovarian cancer. *The Lancet.* 2014 Oct 17;384(9951):1376–88.
5. Tanaka YO, Okada S, Satoh T, Matsumoto K, Oki A, Saida T, et al. Differentiation of epithelial ovarian cancer subtypes by use of imaging and clinical data: a detailed analysis. *Cancer Imaging.* 2016;16:3.
6. NCCN Guidelines for Patients | Ovarian Cancer [Internet]. [cited 2017 Apr 22]. Available from: <https://www.nccn.org/patients/guidelines/ovarian/index.html#6>
7. How Is Ovarian Cancer Staged? [Internet]. [cited 2017 Apr 22]. Available from: <https://www.cancer.org/cancer/ovarian-cancer/detection-diagnosis-staging/staging.html>
8. Ahmed N, Stenvers KL. Getting to know ovarian cancer ascites: opportunities for targeted therapy-based translational research. *Front Oncol.* 2013 Sep 25;3:256.
9. Zeimet AG, Reimer D, Radl AC, Reinthaller A, Schauer C, Petru E, et al. Pros and cons of intraperitoneal chemotherapy in the treatment of epithelial ovarian cancer. *Anticancer Res.* 2009 Jul;29(7):2803–8.
10. Sangisetty SL, Miner TJ. Malignant ascites: A review of prognostic factors, pathophysiology and therapeutic measures. *World J Gastrointest Surg.* 2012 Apr 27;4(4):87–95.
11. Malik I, Abubakar S, Rizwana I, Alam F, Rizvi J, Khan A. Clinical features and management of malignant ascites. *J Pak Med Assoc.* 1991 Feb;41(2):38–40.
12. Bala L, Sharma A, Yellapa RK, Roy R, Choudhuri G, Khetrpal CL. (1)H NMR spectroscopy of ascitic fluid: discrimination between malignant and benign ascites and comparison of the results with conventional methods. *NMR Biomed.* 2008 Jul;21(6):606–14.
13. Huang H, Li YJ, Lan CY, Huang QD, Feng YL, Huang YW, et al. Clinical significance of ascites in epithelial ovarian cancer. *Neoplasma.* 2013;60(5):546–52.

14. Tomczak K, Czerwińska P, Wiznerowicz M. The Cancer Genome Atlas (TCGA): an immeasurable source of knowledge. *Contemp Oncol (Pozn)*. 2015;19(1A):A68–77.
15. TCGA Completes Ovarian Cancer Analysis [Internet]. The Cancer Genome Atlas - National Cancer Institute. [cited 2017 Apr 23]. Available from: <https://cancergenome.nih.gov/newsevents/newsannouncements/ovarianpaper>
16. Yuan Y, Van Allen EM, Omberg L, Wagle N, Amin-Mansour A, Sokolov A, et al. Assessing the clinical utility of cancer genomic and proteomic data across tumor types. *Nat Biotech*. 2014 Jul;32(7):644–52.
17. Denkert C, Budczies J, Darb-Esfahani S, Györfy B, Sehouli J, Könsgen D, et al. A prognostic gene expression index in ovarian cancer - validation across different independent data sets. *J Pathol*. 2009 Jun;218(2):273–80.
18. Network TCGAR. Integrated genomic analyses of ovarian carcinoma. *Nature*. 2011 Jun 30;474(7353):609–15.
19. TXNIP Gene - GeneCards | TXNIP Protein | TXNIP Antibody [Internet]. [cited 2017 Apr 26]. Available from: <http://www.genecards.org/cgi-bin/carddisp.pl?gene=TXNIP>
20. Yamaguchi F, Takata M, Kamitori K, Nonaka M, Dong Y, Sui L, et al. Rare sugar D-allose induces specific up-regulation of TXNIP and subsequent G1 cell cycle arrest in hepatocellular carcinoma cells by stabilization of p27kip1. *Int J Oncol*. 2008 Feb;32(2):377–85.
21. Yoshihara E, Masaki S, Matsuo Y, Chen Z, Tian H, Yodoi J. Thioredoxin/Txnip: redoxisome, as a redox switch for the pathogenesis of diseases. *Front Immunol*. 2014 Jan 9;4:514.
22. Jin H-O, Seo S-K, Kim Y-S, Woo S-H, Lee K-H, Yi J-Y, et al. TXNIP potentiates Redd1-induced mTOR suppression through stabilization of Redd1. *Oncogene*. 2011 Sep 1;30(35):3792–801.
23. Saxena G, Chen J, Shalev A. Intracellular Shuttling and Mitochondrial Function of Thioredoxin-interacting Protein. *J Biol Chem*. 2010 Feb 5;285(6):3997–4005.
24. Takahashi Y, Ishii Y, Murata A, Nagata T, Asai S. Localization of thioredoxin-interacting protein (TXNIP) mRNA in epithelium of human gastrointestinal tract. *J Histochem Cytochem*. 2003 Jul;51(7):973–6.
25. Ogata FT, Batista WL, Sartori A, Gesteira TF, Masutani H, Arai RJ, et al. Nitrosative/Oxidative Stress Conditions Regulate Thioredoxin-Interacting Protein (TXNIP) Expression and Thioredoxin-1 (TRX-1) Nuclear Localization. *PLOS ONE*. 2013 Dec 20;8(12):e84588.
26. Shen L, O’Shea JM, Kaadige MR, Cunha S, Wilde BR, Cohen AL, et al. Metabolic reprogramming in triple-negative breast cancer through Myc suppression of TXNIP. *Proc Natl Acad Sci USA*. 2015 Apr 28;112(17):5425–30.
27. Zhou J, Chng W-J. Roles of thioredoxin binding protein (TXNIP) in oxidative stress, apoptosis and cancer. *Mitochondrion*. 2013 May;13(3):163–9.
28. Li Y, Miao L-Y, Xiao Y-L, Huang M, Yu M, Meng K, et al. Hypoxia induced high expression of thioredoxin interacting protein (TXNIP) in non-small cell lung cancer and its prognostic effect. *Asian Pac J Cancer Prev*. 2015;16(7):2953–8.

29. Mohapatra S, Nandi S, Chowdhury R, Das G, Ghosh S, Bhattacharyya K. Spectral mapping of 3D multi-cellular tumor spheroids: time-resolved confocal microscopy. *Phys Chem Chem Phys*. 2016 Jul 21;18(27):18381–90.
30. le Roux L, Volgin A, Maxwell D, Ishihara K, Gelovani J, Schellingerhout D. Optimizing imaging of three-dimensional multicellular tumor spheroids with fluorescent reporter proteins using confocal microscopy. *Mol Imaging*. 2008 Oct;7(5):214–21.
31. Fennema E, Rivron N, Rouwkema J, van Blitterswijk C, de Boer J. Spheroid culture as a tool for creating 3D complex tissues. *Trends Biotechnol*. 2013 Feb;31(2):108–15.
32. Hongisto V, Jernström S, Fey V, Mpindi J-P, Kleivi Sahlberg K, Kallioniemi O, et al. High-throughput 3D screening reveals differences in drug sensitivities between culture models of JIMT1 breast cancer cells. *PLoS ONE*. 2013;8(10):e77232.
33. Schindelin J, Arganda-Carreras I, Frise E, Kaynig V, Longair M, Pietzsch T, et al. Fiji: an open-source platform for biological-image analysis. *Nat Methods*. 2012 Jun 28;9(7):676–82.
34. Gyorffy B, Lanczky A, Szallasi Z. Implementing an online tool for genome-wide validation of survival-associated biomarkers in ovarian-cancer using microarray data of 1287 patients, *Endocrine-Related Cancer*. 2012 Apr 10;19(2):197-208.
35. Chen JL, David J, Cook-Spaeth D, Casey S, Cohen D, Selvendiran K, et al. Autophagy Induction Results in Enhanced Anoikis Resistance in Models of Peritoneal Disease. *Mol Cancer Res*. 2017 Jan;15(1):26–34.

Appendix A: Tables and Figures

Figure 1: Model of peritoneal metastasis

Illustration of the *in vitro* model for peritoneal metastasis used in this study.

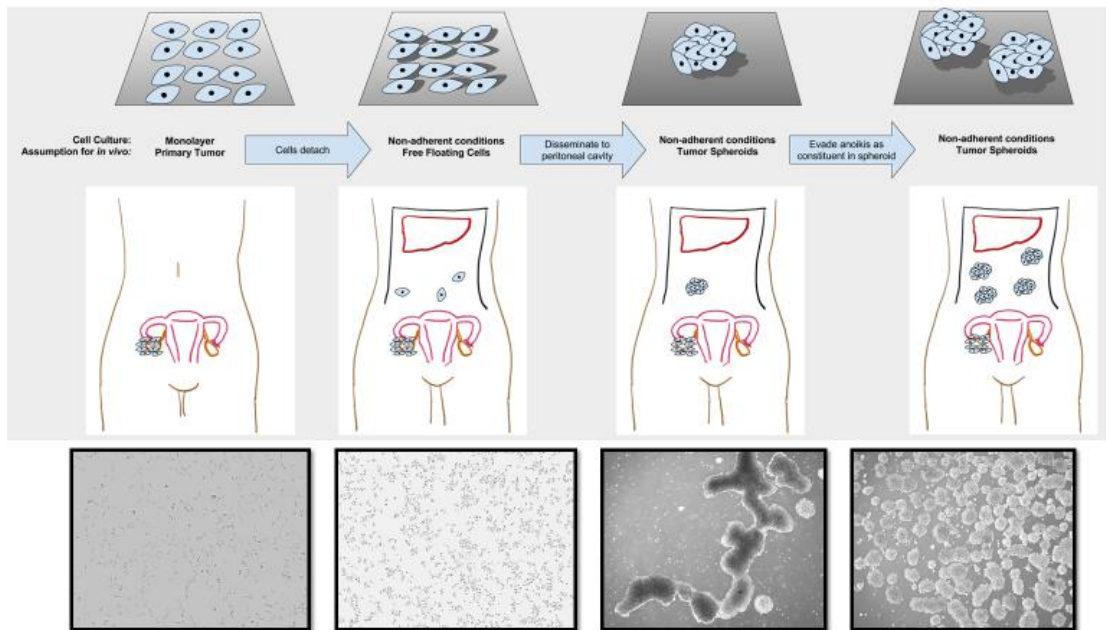


Figure 2: Overview of study design

A brief overview of the study design.

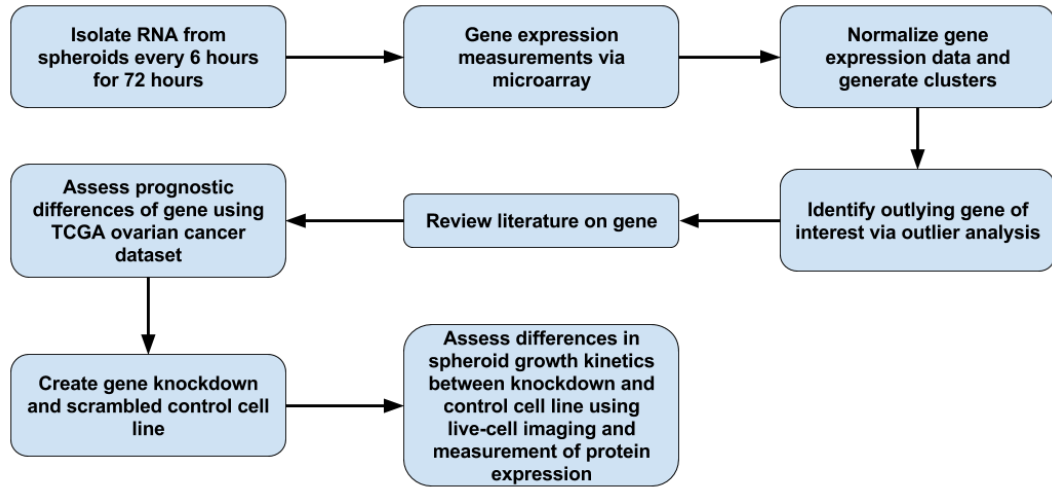


Figure 3: Z-stack generated with confocal microscopy

Z-stacks of GFP-tagged HeyA8 spheroids obtained using confocal microscopy.

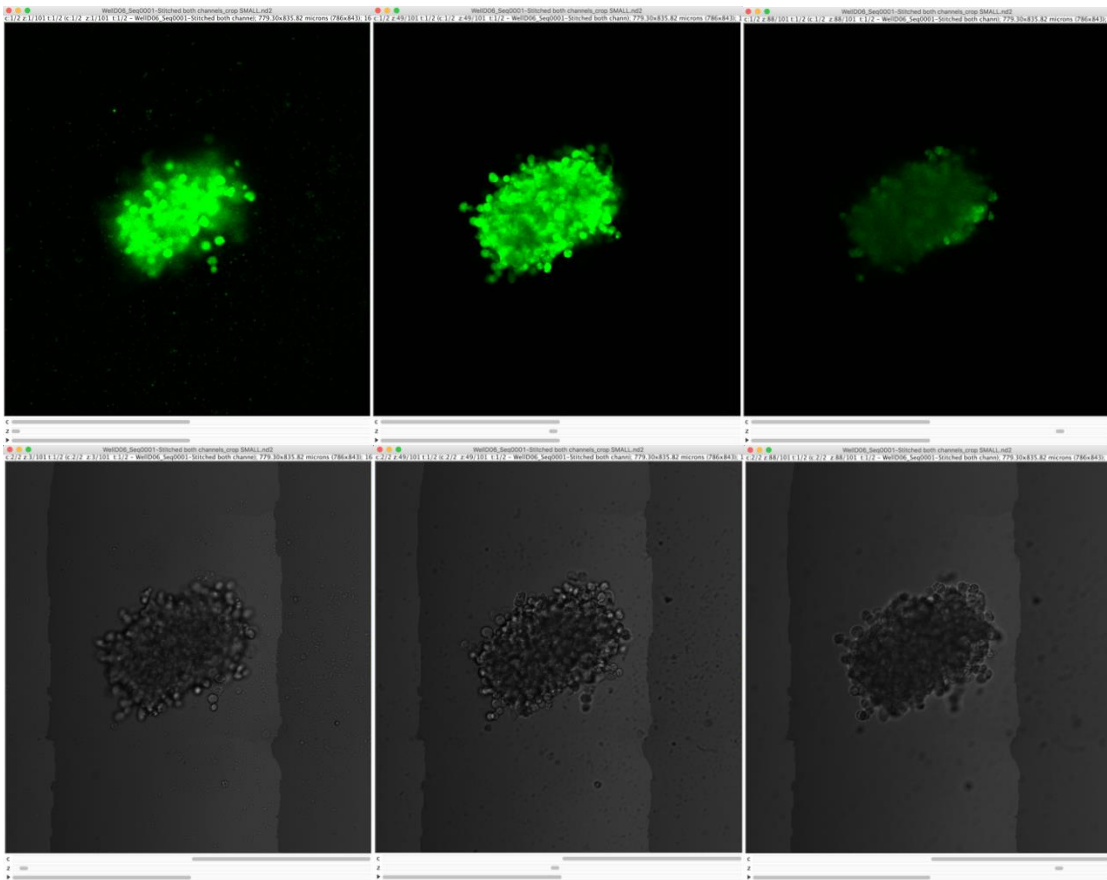
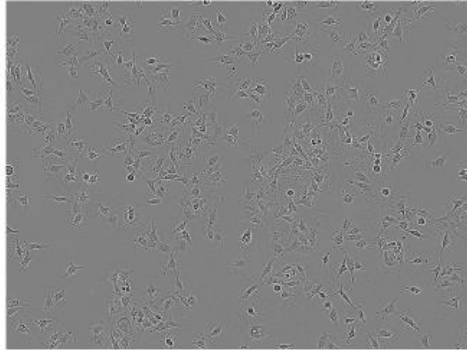


Figure 4: Example of pixel masking

An example of pixel masking performed on attached cells.

10x Brightfield Image



After analysis + masking

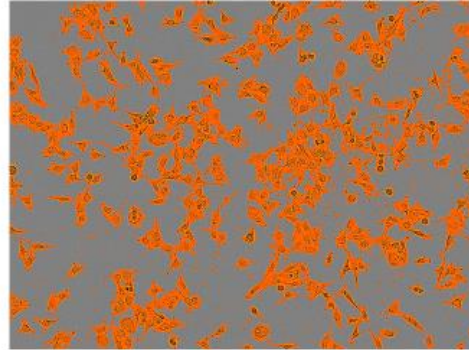


Figure 5: Image analysis workflow

Image analysis workflow used to obtain quantitative growth metrics for spheroids.

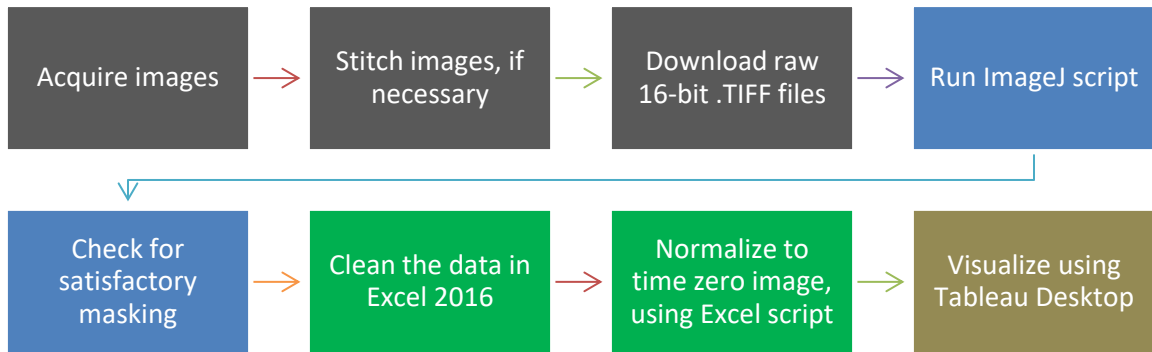
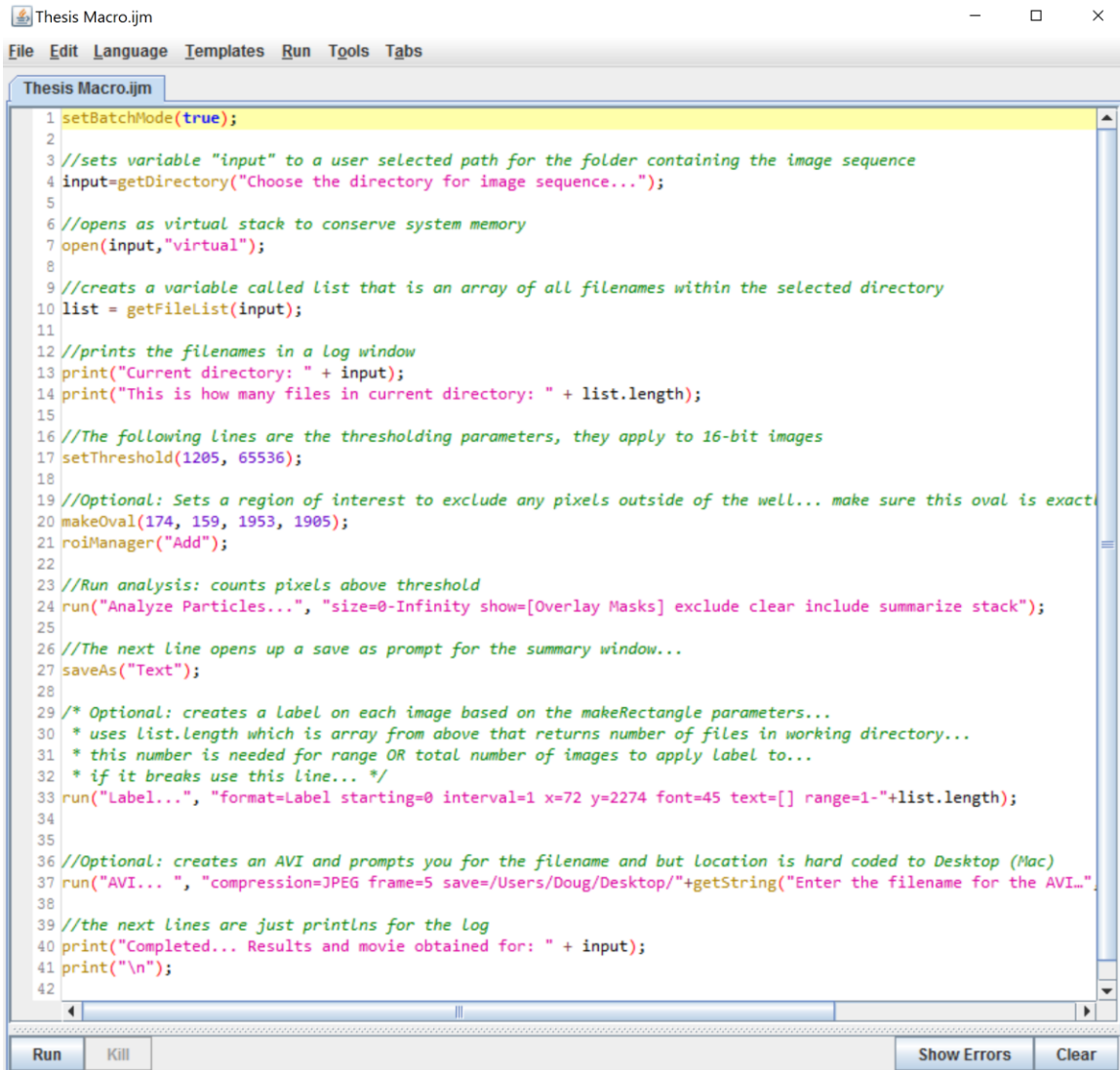


Figure 6: ImageJ macro

The script used to threshold and quantify images in ImageJ.



```
1 setBatchMode(true);
2
3 //sets variable "input" to a user selected path for the folder containing the image sequence
4 input=getDirectory("Choose the directory for image sequence...");
5
6 //opens as virtual stack to conserve system memory
7 open(input,"virtual");
8
9 //creates a variable called list that is an array of all filenames within the selected directory
10 list = getFileList(input);
11
12 //prints the filenames in a log window
13 print("Current directory: " + input);
14 print("This is how many files in current directory: " + list.length);
15
16 //The following lines are the thresholding parameters, they apply to 16-bit images
17 setThreshold(1205, 65536);
18
19 //Optional: Sets a region of interest to exclude any pixels outside of the well... make sure this oval is exact
20 makeOval(174, 159, 1953, 1905);
21 roiManager("Add");
22
23 //Run analysis: counts pixels above threshold
24 run("Analyze Particles...", "size=0-Infinity show=[Overlay Masks] exclude clear include summarize stack");
25
26 //The next line opens up a save as prompt for the summary window...
27 saveAs("Text");
28
29 /* Optional: creates a label on each image based on the makeRectangle parameters...
30 * uses list.length which is array from above that returns number of files in working directory...
31 * this number is needed for range OR total number of images to apply label to...
32 * if it breaks use this line... */
33 run("Label...", "format=Label starting=0 interval=1 x=72 y=2274 font=45 text=[] range=1-"+list.length);
34
35
36 //Optional: creates an AVI and prompts you for the filename and but location is hard coded to Desktop (Mac)
37 run("AVI... ", "compression=JPEG frame=5 save=/Users/Doug/Desktop/"+getString("Enter the filename for the AVI..."));
38
39 //the next lines are just printlns for the log
40 print("Completed... Results and movie obtained for: " + input);
41 print("\n");
42
```

Figure 7: Inter-experimental variability in non-adherent conditions

Graph showing inter-experimental variability after the removal of two trials that showed inconsistent masking resulting in overly jagged curves that are not biologically representative. The inconsistent masking could have been due to fluctuations in the instrument, trouble with auto-focus, or the selection of an inappropriate threshold value.

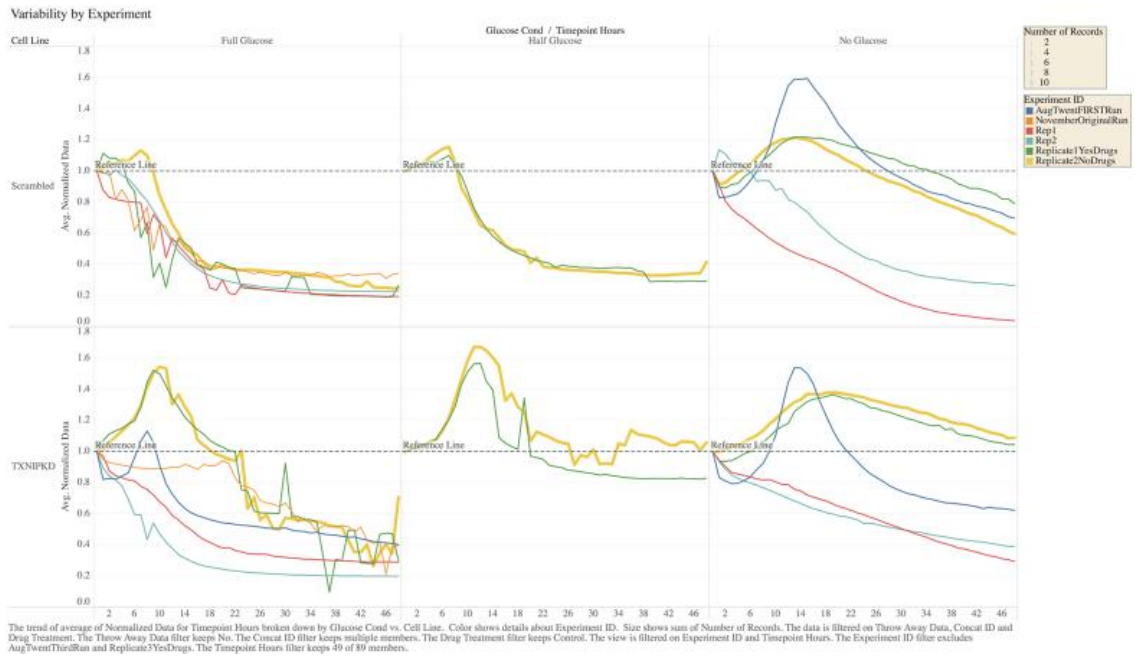


Figure 8: Averages of total spheroid area versus time

Six dual-axis graphs showing the average of total spheroid area versus time across glucose conditions and cell lines. The left y-axis shows average spheroid area versus time, indicated by red lines. The right y-axis shows relative standard error of the mean versus time, indicated by grey lines.

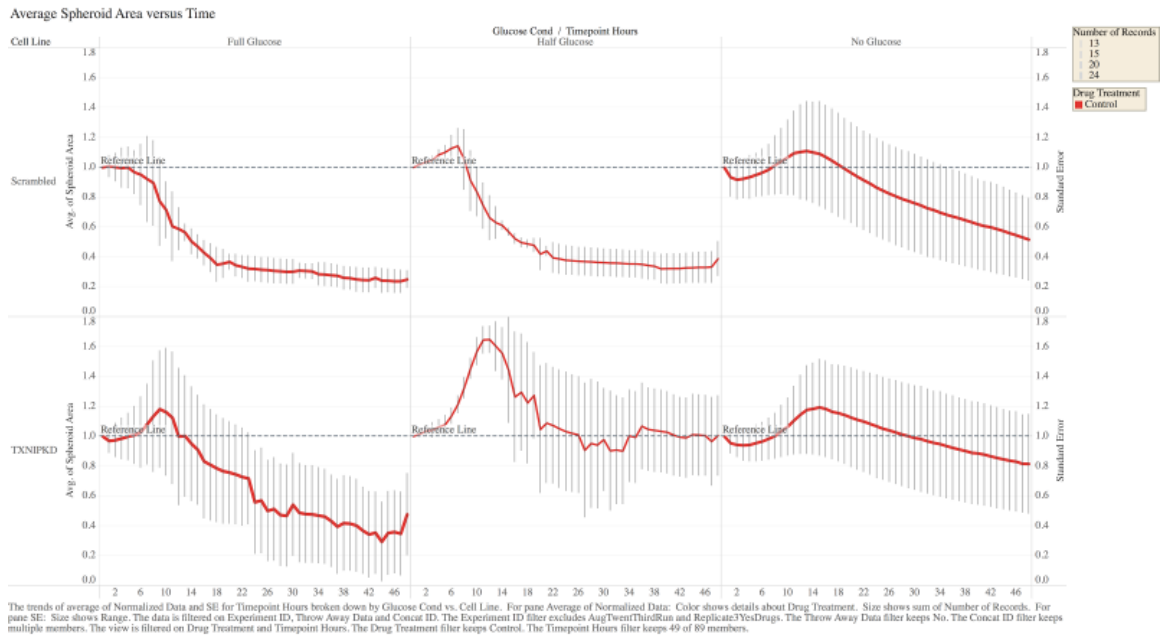
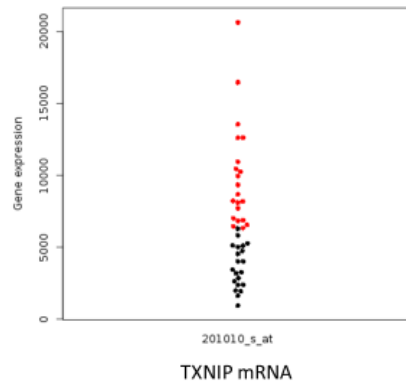


Figure 9: Beeswarm plots

Beeswarm plots showing the distribution of mRNA expression levels within early and late stage patients that are members of the TCGA ovarian cancer dataset. The red indicates expression above the median, the black indicates expression below or equal to the median expression value.

Variance in mRNA expression - Beeswarm plot

Stage 1 & 2 (N = 42)



Stage 3 & 4 (N = 331)

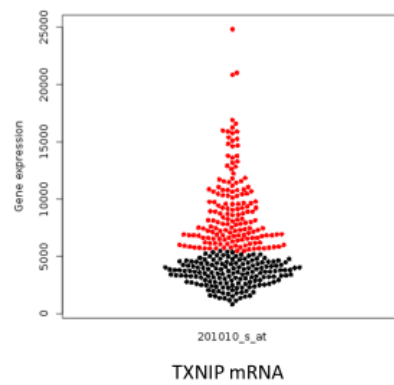


Figure 10: Clustering

Graph showing TXNIP gene expression relative to the 6 clusters generated using a Gaussian Mixtures Model over 12 time points.

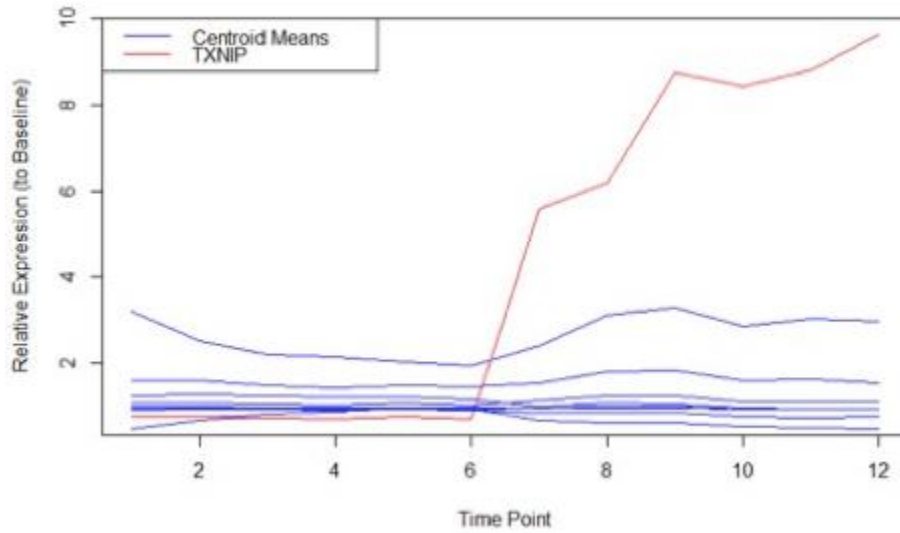


Figure 11: TXNIP mRNA expression versus time in non-adherent conditions.

TXNIP mRNA expression versus time in non-adherent conditions.

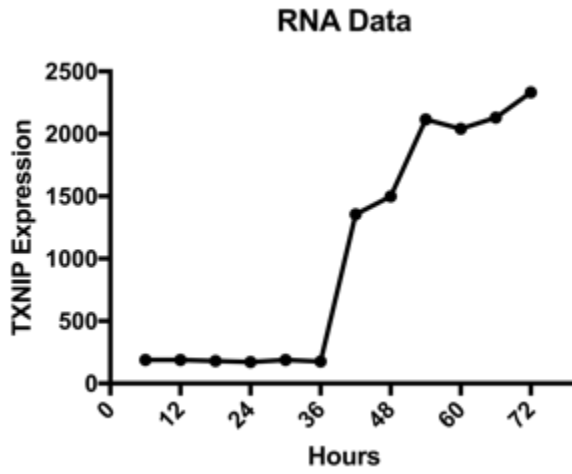


Figure 12: Western blots of knockdown versus control

A) Western blot of HeyA8 TXNIP knockdown and HeyA8 scrambled control cell lines confirming successful knockdown of TXNIP in the knockdown cell line and temporal expression of TXNIP at the protein level in the control. **B)** Pixel densitometry performed on (A) showing 1.79 fold increase in TXNIP expression in the knockdown cell line and 6.59 fold increase in TXNIP expression in the scrambled cell line. **C)** Western blot of HeyA8 TXNIP knockdown versus HeyA8 scrambled control cell lines, again, showing successful knockdown of TXNIP in the knockdown cell line. **D)** Pixel densitometry performed on (C) showing 31% reduction in TXNIP expression in the TXNIP knockdown cell line under attached conditions and a 52% reduction in TXNIP expression in the TXNIP knockdown cell line in non-adherent conditions, as compared to control.

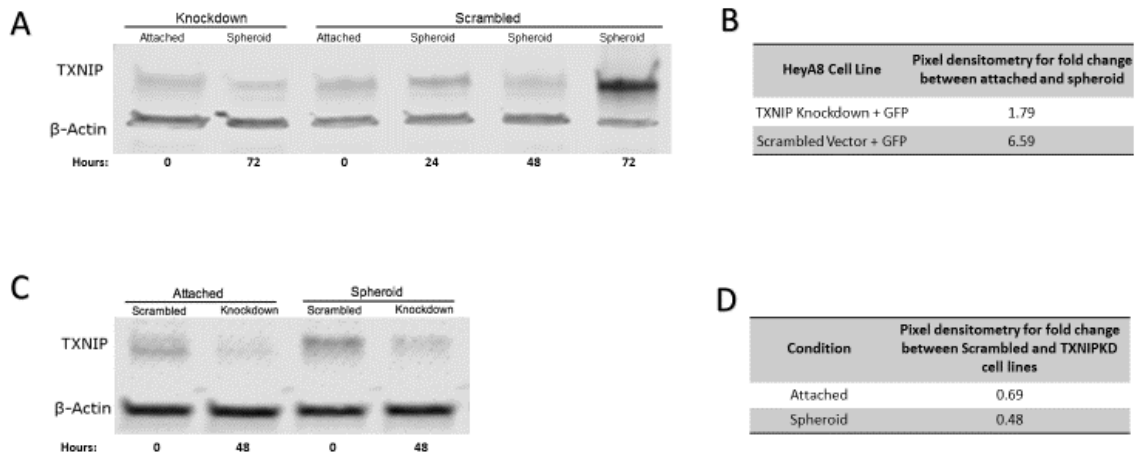


Figure 13: Three-dimensional reconstruction of HeyA8 spheroids.

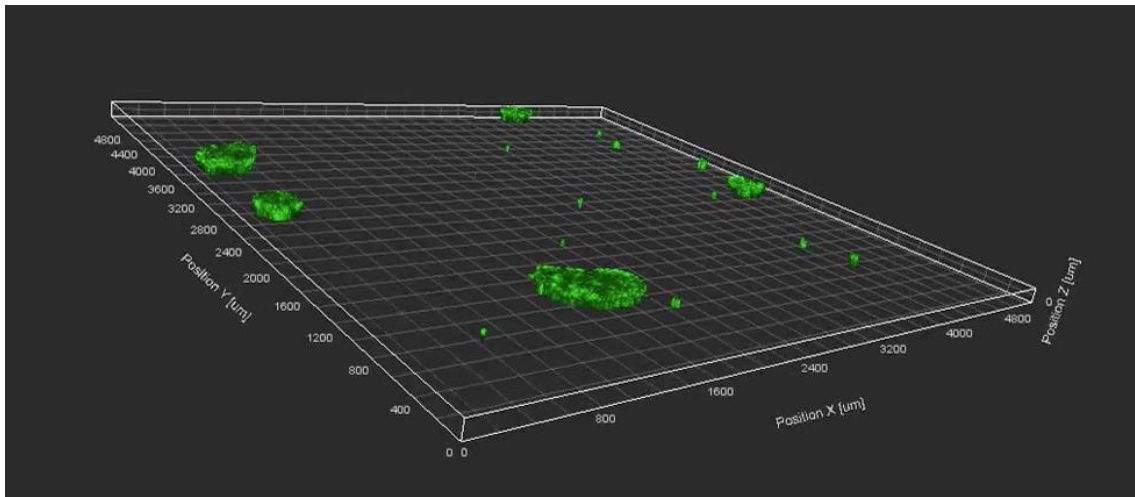


Figure 14: Comparisons of knockdown and control at 48 hours

Left: Bar chart comparing percent confluency at 48 hours between scrambled and TXNIP knockdown cell lines grown as monolayers. *Right:* Bar chart comparing normalized total green area at 48 hours between scrambled and TXNIP knockdown cell lines grown under non-adherent conditions.

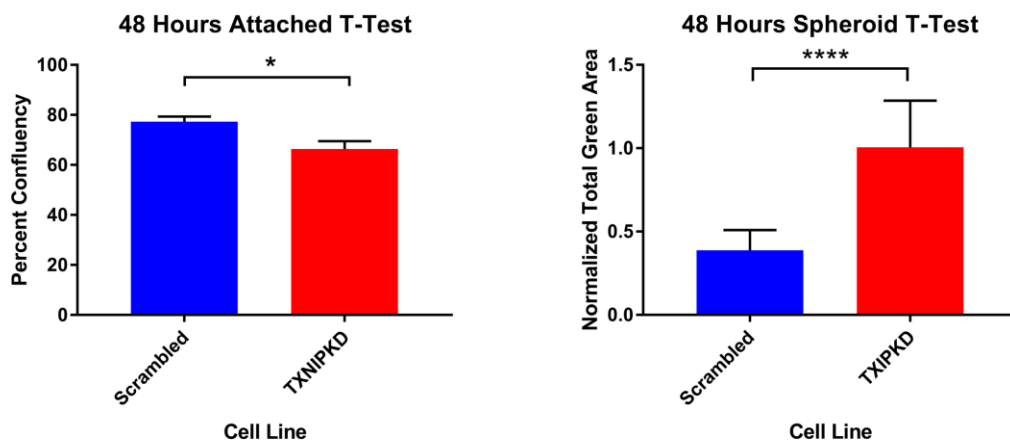


Figure 15: Plot of confluency versus time for knockdown and control

Graph plotting percent confluence over time for scrambled and TXNIP knockdown cell lines.

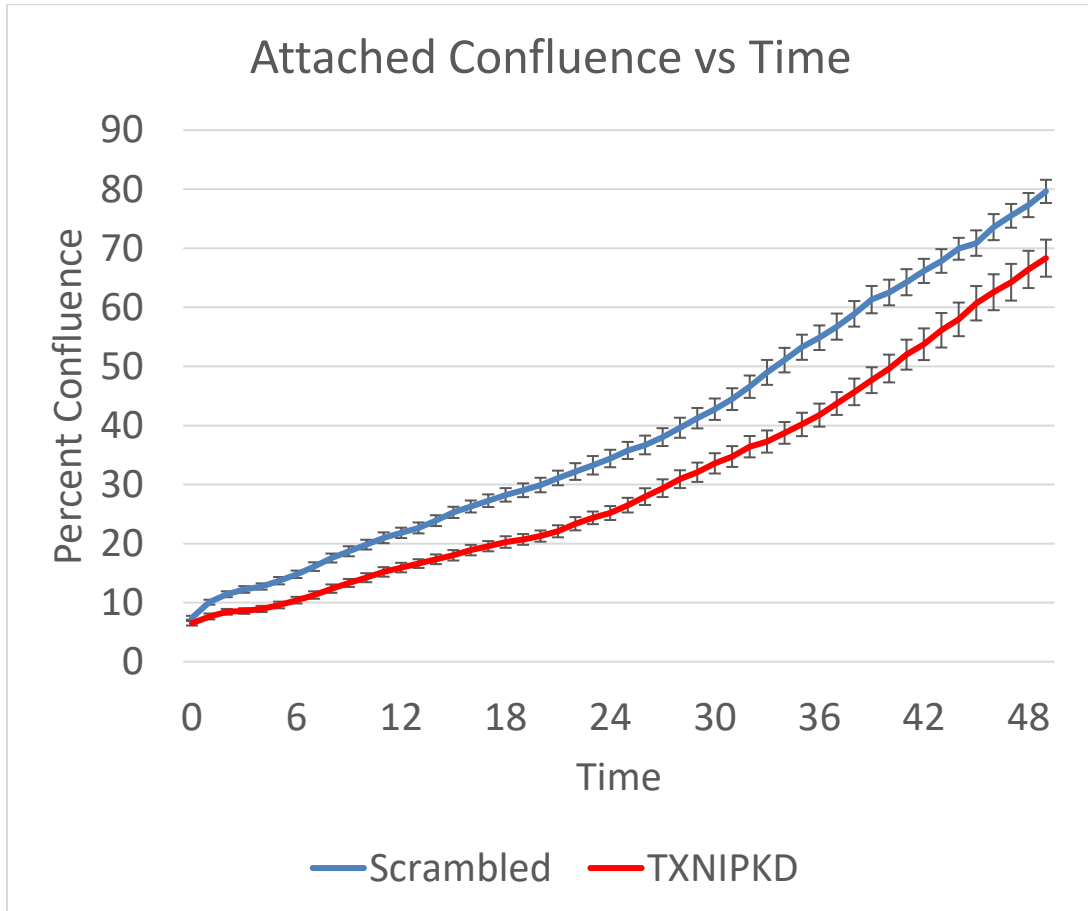


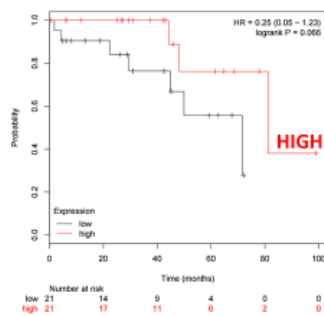
Figure 16: Kaplan-Meier plots

TCGA ovarian cancer dataset survival analysis of early and late stage patients split by median TXNIP expression.

Overall Survival

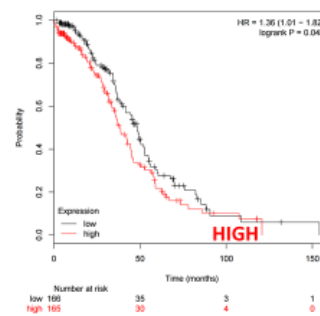
Stage 1 and 2

- TXNIP High Lives Longer



Stage 3 and 4

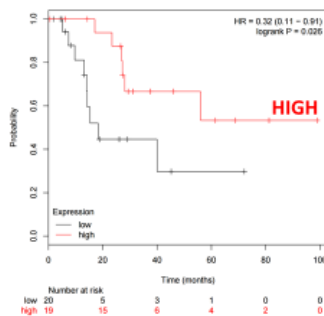
- TXNIP High Dies Earlier



Progression Free Survival

Stage 1 and 2

- TXNIP High Progresses Later



Stage 3 and 4

- TXNIP High Progresses Faster

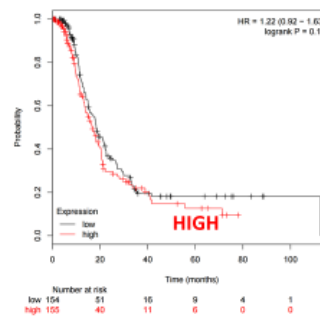


Figure 17: Western blot showing effect of carboplatin on TXNIP expression
Western blot for TXNIP in three ovarian cancer cell lines comparing untreated versus 100 nM carboplatin treated after 48 hours in non-adherent conditions.

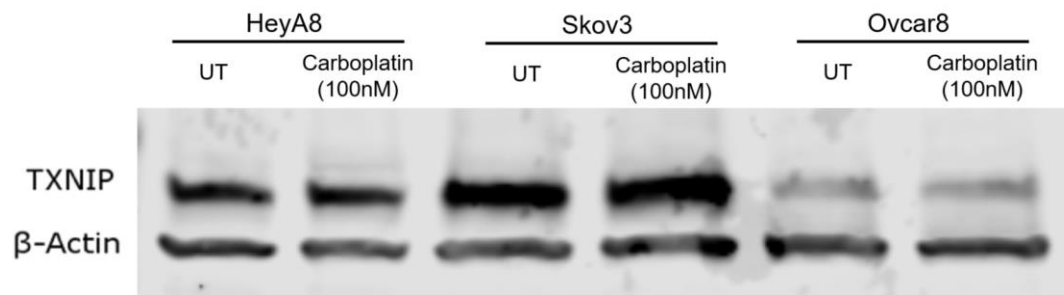


Table 1: Images acquired per experiment

Number of images acquired across all non-adherent experiments by experimental condition.

Images per experiment

Cell Line	AugTwentFIRSTRun	AugTwentThirdRun	NovemberOriginalRun	Experiment ID			Replicate1YesDrugs	Replicate2NoDrugs	Replicate3YesDrugs
				Rep1	Rep2	Rep3			
Scrambled	735	1,470	294	882	882	1,323	1,470	1,323	
TXNIPKD	1,470	1,470	294	882	882	1,323	1,470	1,323	

Number of Records broken down by Experiment ID vs. Cell Line. The data is filtered on Throw Away Data and Early 48 OR Late 72. The Throw Away Data filter keeps No. The Early 48 OR Late 72 filter keeps only images from the first 48 hours.

Images per experiment: by drug

Cell Line	Drug Treatment	AugTwentFIRSTRun	AugTwentThirdRun	NovemberOriginalRun	Experiment ID			Replicate1YesDrugs	Replicate2NoDrugs	Replicate3YesDrugs
					Rep1	Rep2	Rep3			
Scrambled	Chloroquine 50uM	147	294	98	294	294	0	0	0	
	Control	147	294	98	294	294	441	1,470	441	
	MLN0128 50nM	147	294	0	0	0	441	0	441	
	RapaChloroCombo	147	294	0	0	0	0	0	0	
	Rapamycin 50nM	147	294	98	294	294	441	0	441	
TXNIPKD	Chloroquine 50uM	294	294	98	294	294	0	0	0	
	Control	294	294	98	294	294	441	1,470	441	
	MLN0128 50nM	294	294	0	0	0	441	0	441	
	RapaChloroCombo	294	294	0	0	0	0	0	0	
	Rapamycin 50nM	294	294	98	294	294	441	0	441	

Number of Records broken down by Experiment ID vs. Cell Line and Drug Treatment. The data is filtered on Throw Away Data and Early 48 OR Late 72. The Throw Away Data filter keeps No. The Early 48 OR Late 72 filter keeps only images from the first 48 hours.

Images per experiment: by glucose condition

Cell Line	Glucose Cond	AugTwentFIRSTRun	AugTwentThirdRun	NovemberOriginalRun	Experiment ID			Replicate1YesDrugs	Replicate2NoDrugs	Replicate3YesDrugs
					Rep1	Rep2	Rep3			
Scrambled	Full Glucose	0	735	294	441	441	441	490	441	
	Half Glucose	0	0	0	0	0	441	490	441	
	No Glucose	735	735	0	441	441	441	490	441	
TXNIPKD	Full Glucose	735	735	294	441	441	441	490	441	
	Half Glucose	0	0	0	0	0	441	490	441	
	No Glucose	735	735	0	441	441	441	490	441	

Number of Records broken down by Experiment ID vs. Cell Line and Glucose Cond. The data is filtered on Throw Away Data and Early 48 OR Late 72. The Throw Away Data filter keeps No. The Early 48 OR Late 72 filter keeps only images from the first 48 hours.

Table 2: Results of t-tests

Left: Results of t-tests performed on image data from the 48 hour time point for attached conditions. *Right:* Results of t-test performed on image data from the 48 hour time point for non-adherent conditions.

Table Analyzed	48 Hours Attached T-Test
Column B	TXNIPKD
vs.	vs.
Column A	Scrambled
Unpaired t test	
P value	0.0117
P value summary	*
Significantly different (P < 0.05)?	Yes
One- or two-tailed P value?	Two-tailed
t, df	t=2.898 df=14
How big is the difference?	
Mean ± SEM of column A	77.31 ± 2.041, n=8
Mean ± SEM of column B	66.41 ± 3.157, n=8
Difference between means	-10.9 ± 3.759
95% confidence interval	-18.96 to -2.833
R squared (eta squared)	0.375
F test to compare variances	
F, DFn, Dfd	2.391, 7, 7
P value	0.2729
P value summary	ns
Significantly different (P < 0.05)?	No

Table Analyzed	48 Hours Spheroid T-Test
Column B	TXIPKD
vs.	vs.
Column A	Scrambled
Unpaired t test with Welch's correction	
P value	<0.0001
P value summary	****
Significantly different (P < 0.05)?	Yes
One- or two-tailed P value?	Two-tailed
Welch-corrected t, df	t=7.284 df=16.3
How big is the difference?	
Mean ± SEM of column A	0.3884 ± 0.03347, n=13
Mean ± SEM of column B	1.005 ± 0.07778, n=13
Difference between means	0.6168 ± 0.08468
95% confidence interval	0.4375 to 0.796
R squared (eta squared)	0.765
F test to compare variances	
F, DFn, Dfd	5.4, 12, 12
P value	0.0066
P value summary	**
Significantly different (P < 0.05)?	Yes